Twisted bilayer graphene in a parallel magnetic field

Yves H. Kwan and S. A. Parameswaran
Rudolf Peierls Centre for Theoretical Physics, Clarendon Laboratory, Oxford OX1 3PU, UK

S. L. Sondhi
Department of Physics, Princeton University, Princeton, New Jersey 08540, USA
(Dated: April 12, 2020)

We study the effect of an in-plane magnetic field on the non-interacting dispersion of twisted bilayer graphene. Our analysis is rooted in the chirally symmetric continuum model, whose zero-field band structure hosts exactly flat bands and large energy gaps at the magic angles. At the first magic angle, the central bands respond to a parallel field by forming a quadratic band crossing point (QBCP) at the moiré Brillouin zone center. Over a large range of fields, the dispersion is invariant with an overall scale set by the magnetic field strength. For deviations from the magic angle and for realistic interlayer couplings, the motion and merging of the Dirac points lying near charge neutrality are discussed in the context of the symmetries, and we show that small magnetic fields are able to induce a qualitative change in the energy spectrum. We conclude with a discussion on the possible ramifications of our study to the interacting ground states of twisted bilayer graphene systems.

I. INTRODUCTION

Flat band systems allow electron interactions to dominate kinetic energy, providing a favorable setting for exotic correlated and topological phases of matter to emerge [1, 2]. A recent entrant to their roster is twisted bilayer graphene (TBG), a van der Waals heterostructure [3] that, absent interactions, exhibits Dirac points (DPs) at charge neutrality with a suppressed Fermi velocity compared to monolayer graphene [4–10]. The suppression is especially pronounced near small 'magic' twist angles at which the two central moiré bands (per valley and spin) become nearly flat in the moiré Brillouin zone (mBZ) [6]. The rich possibilities this affords to correlation effects are strikingly illustrated by the experimental discovery of proximate Mott insulating and superconducting phases [11, 12], and more recent observations of the anomalous Hall effect and orbital ferromagnetism [13–15]. Concomitantly, a large body of theoretical work has emerged to explain various aspects of TBG and related moiré heterostructures [16–35].

Part of the allure of TBG arises from its remarkable tunability. The smallness of the mBZ allows for gate-induced doping of the flat bands. Hydrostatic pressure increases the interlayer coupling strength and the magic angles [36, 37]. The purely two-dimensional setting allows scanning probes to directly interrogate real-space electronic correlations [38–41]. Here, we consider the effects of another tuning parameter — an in-plane magnetic field. Although first considered in Ref. [42], this has been little explored in the flat band setting [33–35] where, as we show, it plays an enhanced role. Starting from the limit of exactly flat and degenerate bands [24], we find that an infinitesimal in-plane field drives the formation of a quadratic band crossing point (QBCP) [43, 44] at the mBZ center. Strikingly, the shape of the resulting dispersion is invariant for experimentally accessible field strengths, which only set the overall bandwidth. For deviations from this flat band limit, we study the motion and merging of DPs, and extend our analysis to realistic interlayer couplings, showing that qualitative features survive away from the chiral limit. We also explore the interplay between orbital and spin effects of in-plane fields, and contextualize our findings within the interacting states of TBG. *In toto*, our results suggest that parallel fields offer an intriguing new 'knob' to explore this intriguing class of moiré materials.

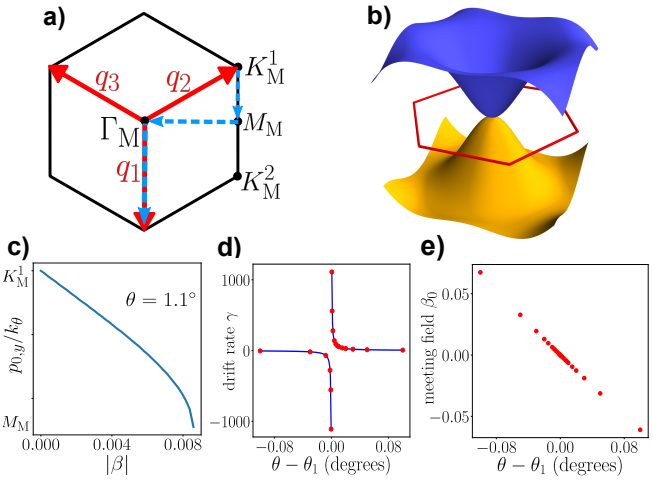

FIG. 1. (a) Moiré Brillouin zone. The moiré and Dirac wavevectors are $k_\theta = 2k_D \sin(\theta/2)$ and $k_D = \frac{4\pi}{3\sqrt{3}a}$ with $a = 1.42$Å the C–C bond length. Blue dashed lines show the mBZ path used for Fig. 2. (b) Central bands at θ_1 in a parallel magnetic field, showing quadratic band crossing point (QBCP) at Γ_M. (c) The position of the DP originally at K_M^1 as the dimensionless magnetic field is increased along the easy direction. (d) The initial dimensionless drift rate of the DP as a function of angle is computed (red dots) and compared to perturbation theory (blue line). (e) Field along $\hat{x}$ required to induce DP merging as a function of angle.

II. TWISTED BILAYER GEOMETRY & CONTINUUM MODEL

Consider AA-stacked bilayer graphene with interlayer spacing $c_0 = 3.35$ Å. Layers 1 and 2 are placed at $z = \pm c_0/2$ and rotated by $\pm\theta/2$ respectively about a hexagon

center; this choice preserves the maximal subset of monolayer symmetries including C_{6v} rotation about the hexagon center [17]. Generic twist angles lead to an incommensurate structure. However, the "continuum approximation" [6] yields a Hamiltonian that is periodic with moiré wavevector $k_\theta = 2k_D \sin\theta/2$ [45], and furthermore promotes the approximate valley $U(1)$ to an exact symmetry. Restricting to states near monolayer valley K, the intralayer physics is captured by Dirac dispersions centered at $\boldsymbol{K}^{1,2} \equiv R_{\pm\theta/2}\boldsymbol{K}$. These momenta fold onto mBZ corners (Fig. 1) upon including interlayer coupling in the dominant harmonic approximation [6]. In the Bloch spinor basis $\psi(\boldsymbol{p}) = [\psi_{1A}(\boldsymbol{p}), \psi_{1B}(\boldsymbol{p}), \psi_{2A}(\boldsymbol{p}), \psi_{2B}(\boldsymbol{p})]^T$ with $\boldsymbol{p}$ measured relative to the DP the Hamiltonian is

$$H(\boldsymbol{p},\boldsymbol{p}') = \begin{pmatrix} \hbar v_0 \boldsymbol{\sigma}^*_{\theta/2}\cdot\boldsymbol{p}\,\delta_{\boldsymbol{p},\boldsymbol{p}'} & \sum_{i=j}^3 T_j \delta_{\boldsymbol{p}-\boldsymbol{p}',\boldsymbol{q}_j} \\ \sum_{i=j}^3 T_j \delta_{\boldsymbol{p}-\boldsymbol{p}',-\boldsymbol{q}_j} & \hbar v_0 \boldsymbol{\sigma}^*_{-\theta/2}\cdot\boldsymbol{p}\,\delta_{\boldsymbol{p},\boldsymbol{p}'} \end{pmatrix} \quad (1)$$

where $v_0 = 8.8 \times 10^5$ ms^{-1} is the bare Fermi velocity, the Pauli matrices act in sublattice space, $\boldsymbol{\sigma}_{\theta/2} = e^{i\theta\sigma_z/4}\boldsymbol{\sigma}e^{-i\theta\sigma_z/4}$, $T_j = w_{AA}\sigma^0 + w_{AB}(\cos\frac{2\pi(j-1)}{3}\sigma^x + \sin\frac{2\pi(j-1)}{3}\sigma^y)$, and the $\boldsymbol{q}_j$ are given in Fig. 1(a). w_{AA} (w_{AB}) parameterizes the AA/BB (AB/BA) interlayer hopping strengths, and $w_{AA} < w_{AB}$ due to lattice relaxation effects [46, 47]. The interlayer coupling leads to downward renormalization of the Fermi velocity, especially near the magic angles $\{\theta_m\}$.

For $w_{AA} = 0$ [24], the model acquires a chiral/particle-hole symmetry because $\{H, \sigma_z\} = 0$. Its spectrum depends only on the dimensionless angle parameter $\alpha \equiv w_{AB}/v_0\hbar k_\theta$, where $w_{AB} = 0.11$ eV. Remarkably, the two central bands become degenerate, exactly flat, and energetically isolated across the mBZ at the magic angles. We will initially focus on this idealized limit, and consider twists near the first magic angle $\theta_1 \simeq 1.086°$.

III. IN-PLANE FIELD

Orbital effects of an in-plane magnetic field $\boldsymbol{B} = B(\cos\chi, \sin\chi, 0)$ can be incorporated by minimally coupling kinetic terms to a vector potential $\boldsymbol{A} = z\boldsymbol{B}\times\hat{\boldsymbol{z}}$ chosen to preserve the moiré periodicity:

$$\boldsymbol{\sigma}^*_{\pm\theta/2}\cdot\boldsymbol{p} \mapsto \boldsymbol{\sigma}^*_{\pm\theta/2}\cdot\left[\boldsymbol{k} - \boldsymbol{K}^l \pm \frac{eBc_0}{2\hbar}\begin{pmatrix}\sin\chi\\ -\cos\chi\end{pmatrix}\right] \quad (2)$$

where we take upper (lower) signs for layer $l = 1$ ($l = 2$).

Symmetries mandate that the system remains semimetallic for nonzero magnetic field. For $\boldsymbol{B} = 0$ TBG hosts two DPs which are pinned at the mBZ corners $K_M^{1,2}$ due to $\hat{C}_{3v}$ symmetry. Combined time-reversal (TRS) and two-fold rotation $\hat{C}_{2v}\hat{\mathcal{T}}$ (realized as $\sigma_x\hat{\mathcal{K}}\{\boldsymbol{r}\to-\boldsymbol{r}\}$, where $\hat{\mathcal{K}}$ is complex conjugation) quantizes the Berry phase to 0 or π, endowing the DPs with a $\mathbb{Z}_2$ charge and protecting them from gapping out individually [48]. A stronger condition holds as long as the central pair of bands are energetically isolated: because the DPs arise from the same valley, they can be assigned identical $\mathbb{Z}$ winding numbers which are protected in a two-band model; hence they cannot annihilate unless they touch other bands [16, 48–50].

An in-plane magnetic field preserves $\hat{C}_{2v}\hat{\mathcal{T}}$, since $\hat{C}_{2v}$ and $\hat{\mathcal{T}}$ each flip the field direction. Furthermore, chiral symmetry is preserved so the DPs remain at charge neutrality. However, any field orientation breaks $\hat{C}_{3v}$, meaning the DPs are no longer pinned to the mBZ corners. Therefore we expect them to drift around the mBZ as the magnetic field is ramped up. Since TRS is explicitly broken, the band structure for the K and K' valleys are no longer time-reversed versions of each other.

Intuitively, we can understand this drift in the limit of uncoupled layers [51]: from Eq. (2) we read off that the DPs of two layers are shifted in opposite directions by $\delta\boldsymbol{k} \propto B$. Since they cannot annihilate, it is natural to expect the most interesting effects when they meet. This is easiest to arrange for the field orientation $\boldsymbol{B} = B\hat{x}$, where for $B < 0$ the DPs move towards (away) from each other along $\hat{k}_y$ in valley K (K'). For decoupled layers, the fields required are prohibitively large. However, a simple estimate yields a characteristic field energy scale of $ec_0v_0 \sim 0.3\,\mathrm{meV\cdot T^{-1}}$, indicating that in the flat band limit where the competing energy scale (i.e., the bandwidth) is small, the relative impact of a parallel field can be significant.

A. Behavior at the first magic angle

At the first magic angle θ_1, the central bands of chirally-symmetric TBG are exactly flat and degenerate across the mBZ. As soon as a finite field along any in-plane direction is applied, the bands gap and disperse across the entire mBZ except for a QBCP at Γ_M which lies at charge neutrality [Fig. 1(b) — i.e., the two incipient DPs immediately migrate to the center of the mBZ. Strikingly, the shape of the spectrum is invariant over a remarkably large range of B, which simply sets the overall energy scale [Fig. 2(a)].

We can understand this behavior using degenerate perturbation theory, which gives the energy shift to linear order in B. The lack of a competing kinetic energy explains the persistence of the shape of the spectrum. That the bands touch at Γ_M can be understood using point-group symmetry, as follows. The central bands at Γ_M (which enjoys all single-valley symmetries) transform as singlets. However, the perturbation in (2) transforms as the 2D irreducible representation. Therefore the energies at Γ_M are unchanged to $O(B)$. The band touching is quadratic since there needs to be a net 2π pseudospin winding for it to split into two DPs, and the chiral symmetry rules out a trivial linearly dispersing term.

Magnetic field scales eBc_0v_0 comparable to the $\sim$ 100 meV gap to the nearest bands (corresponding to $B \gtrsim$ 100 T) allow significant interband mixing. This violates the emergent protection of the QBCP, allowing it to split. For finite w_{AA} or $|\theta - \theta_1|$, the low-field band evolution is no longer shape-invariant, since the $B = 0$ bandwidth W provides a new scale. However for small deviations from the exactly flat limit, the spectrum recovers an approximate QBCP for

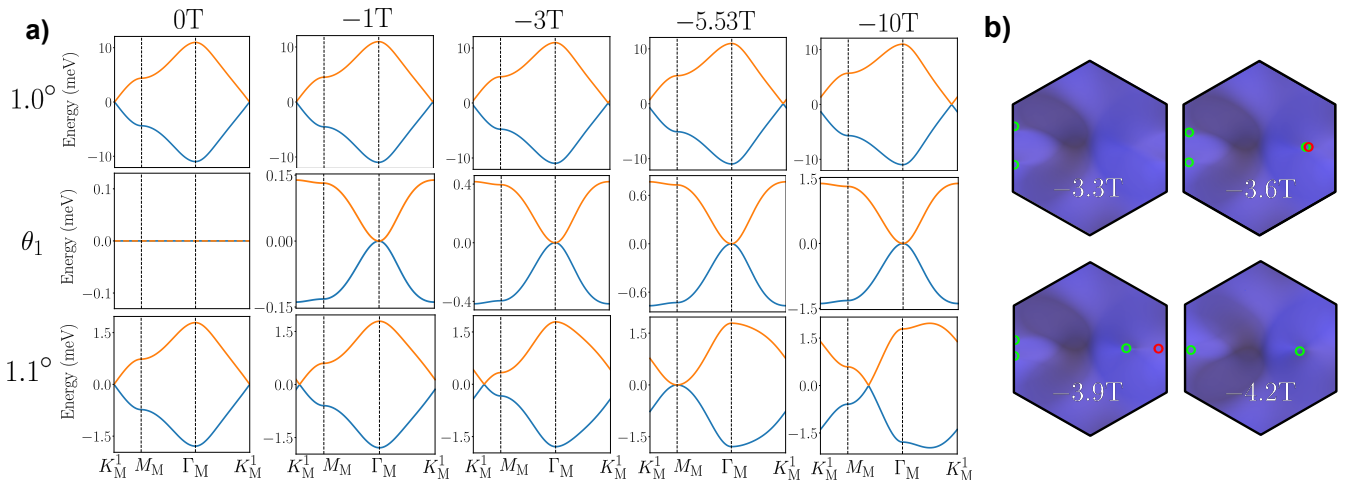

FIG. 2. (a) The central bands of the chirally symmetric model ($w_{AA} = 0$) along $K_{\rm M}^1 \to M_{\rm M} \to \Gamma_{\rm M} \to K_{\rm M}^1$ [see Fig. 1(a)]. The nearest bands are separated by ~ 100 meV. (b) Evolution of DPs in the mBZ (black hexagon), for $w_{AA} = 0.06$ eV and $\theta = 1.1^\circ$. Green/red circles correspond to ± 1 winding number.

$B \gg W/ec_0v_0 \sim 1.5$ T for typical samples at the magic angle where $W \sim 5$ meV.

B. DP motion away from θ_1

Fig. 2(a) displays the evolution of the band structure of chiral TBG close to θ_1 with changing $\boldsymbol{B} = B\hat{x}$. The path in the mBZ [Fig. 1(a)] has been chosen to track the DP originally at $K_{\rm M}^1$. The location of the other DP is determined since two-fold rotation about the x-axis is a symmetry. Actually for vanishing w_{AA} and $\boldsymbol{B} \parallel \hat{x}$, we note that there is another symmetry which demands that $E(k_x, k_y) = -E(-k_x, k_y)$, where $\boldsymbol{k}$ is measured from $\Gamma_{\rm M}$. This is because the spinor part of the kinetic terms can be unrotated for $w_{AA} = 0$ by a unitary transform, leading to a particle-hole symmetry operator of the form $\sigma_y\{k_x \to -k_x\}$. Taken together, these imply that the spectrum is invariant under reflection in k_x and k_y, strongly constraining the motion of the DPs.

The DPs drift along $\hat{k}_y$ for small magnetic fields. As they approach each other, the associated van Hove singularities appear at lower energy. However there are several key differences to the uncoupled layer case. The direction in which the DPs move changes sign across θ_1, and the magnitude of the drift varies non-linearly with B. Furthermore, the rate of drift with B is greater for angles close to θ_1, and appears to diverge as the magic angle is approached.

When the DPs meet at $M_{\rm M}$, they form a QBCP instead of gapping out. When $|B|$ is increased further, the QBCP splits into two DPs that move along $\hat{k}_x$ and drift towards $\Gamma_{\rm M}$. This merging transition of DPs with the same winding has been discussed previously in the context of rotational and stacking defaults in graphene-based systems [52–54]. The DPs do not reach $\Gamma_{\rm M}$, even for large $|B|$ and instead eventually reverse direction. Their point of closest approach can be roughly estimated in terms of the energy scale of the $B = 0$ gap at $\Gamma_{\rm M}$.

If the magnetic field is opposite to the 'easy' direction, for example the case of $\theta < \theta_1$ and $B < 0$ as shown in the top row in Fig. 2(a), the DPs drift vertically towards $\Gamma_{\rm M}$ but do not reach it. Note that the situation in valley K' is time-reversed.

C. Perturbation theory about $K_{\rm M}^1$

Analytical predictions for DP motion can be obtained by considering a truncated version of Eq. (1). Define the dimensionless magnetic field $\beta = eBc_0/\hbar k_\theta$. For small fields, there is a DP located at $\boldsymbol{K}^1 + \boldsymbol{p}_0(\beta)$ with $\boldsymbol{p}_0(\beta)$ parametrically small in β. Therefore we focus on the plane wave state $|\boldsymbol{K}^1 + \boldsymbol{p}, 1\rangle$ with $\boldsymbol{p} \simeq 0$, which directly couples to $|\boldsymbol{K}^2 + \boldsymbol{p} - \boldsymbol{q}_1, 2\rangle$, $|\boldsymbol{K}^2 + \boldsymbol{p} - \boldsymbol{q}_2, 2\rangle$, and $|\boldsymbol{K}^2 + \boldsymbol{p} - \boldsymbol{q}_3, 2\rangle$. The simplest non-trivial approximation includes only these states, thereby defining an effective 8-band model [6]. For $\boldsymbol{p} = 0$ and $\beta = 0$, the Hamiltonian has two zero energy modes, which are the two degenerate states at the DP. By considering the $\boldsymbol{p}$ and β-dependent terms as perturbations, first-order degenerate perturbation theory predicts that the DP moves to a new position $\boldsymbol{p}_0(\beta) = (0, \beta v_0 k_\theta/2v^*)$, with a field-independent renormalized Fermi velocity $v^* = \frac{1-3\alpha^2}{1+3\alpha^2} v_0$ [24]. The Dirac slope vanishes at $\alpha^* = 1/\sqrt{3}$ or an angle of $\theta^* \simeq 1.1^\circ$, which is close to $\theta_1 \simeq 1.086^\circ$. This is consistent with the general observation that perturbation theory accesses the first magic angle relatively well. For relatively flat linear bands, a small perturbation in the dispersion can shift the band crossing by a large distance, which explains why $p_0 \sim 1/v^*$. In this framework it is natural to interpret the θ_1 case as DPs drifting infinitely quickly away from the mBZ corners.

We find that the features of Fig. 2(a), namely the direction and magnitude of DP drift near θ_1 for small β, are exhibited within perturbation theory, which predicts that the drift rate diverges as $\sim 1/|\theta - \theta_1|$. Fig. 1(c) charts the DP position as a

function of β for $\theta = 1.1°$, showing that the initial drift is indeed linear. Fig. 1(d) shows the drift rate $\gamma(\theta) \equiv \frac{\partial(p_0/k_\theta)}{\partial\beta}\big|_{\beta=0}$ as a function of angle which agrees with perturbation theory. Note that to quantitatively compare with numerics, we shift the predicted drift rate in θ to adjust for the slightly different magic angle estimate.

D. Perturbation theory about M_{M}

A similar approach can be used to analyze the merging transition of DPs at M_{M}, this time restricting attention to the two momentum states near M_{M} with the smallest intralayer kinetic energies, namely $|\boldsymbol{K}^1 + \boldsymbol{m} + \boldsymbol{p}, 1\rangle$ and $|\boldsymbol{K}^1 + \boldsymbol{m} + \boldsymbol{p}, 2\rangle$, where $\boldsymbol{m} \equiv k_\theta(0, -1/2)^T$ and $\boldsymbol{p} \simeq 0$. The DPs coincide at M_{M} for $\beta_0 = 2\alpha - 1$, implying the scaling $\beta_0 \sim |\theta - \theta^*|$ where $\theta^* \simeq 1.27°$ deviates slightly from the true magic angle $\theta_1 = 1.086°$. The latter is unsurprising given the crudeness of the 4-band approximation. The linear scaling agrees with the numerics in Fig. 1(e).

At DP coincidence, the eigenstates at M_{M} have energies $0, 0, \pm 2\alpha$. We can capture the perturbative effect of $\boldsymbol{p}$ and $\delta \equiv \beta - \beta_0$ [55] via the low-energy effective Hamiltonian

$$H_{\text{eff}} = \frac{1}{2\alpha}\left[\left(\alpha\delta + \frac{p_x^2 - p_y^2}{1 + \frac{\delta}{4\alpha}}\right)\sigma_x + \frac{2p_x p_y}{1 + \frac{\delta}{4\alpha}}\sigma_y\right]. \qquad (3)$$

This matches the form of the "universal Hamiltonian" describing merging of two DPs with the same winding number [54]. At $\delta = 0$, the two central bands touch parabolically at M_{M}. At finite δ, the DPs lie symmetrically along the k_x or k_y axis depending on the sign of δ, and lie at a distance $\sim \sqrt{\delta}$ from M_{M}. Therefore this 4-band model captures the 'right-angle turning' of the DPs, and also the square-root scaling with δ.

E. Finite AA coupling

The chirally symmetric model is an artificial limit of TBG, and a natural question is whether the above phenomenology persists for more realistic values of w_{AA}. Fig. 2(b) shows the drift of DPs at $\theta = 1.1°$ with $w_{AA} = 0.06$ eV. While the chirally symmetric model has a dispersion invariant under $k_x \to -k_x$, this no longer holds with finite w_{AA}. In addition, the lack of particle-hole symmetry means that the DPs now lie at different energies. The DPs initially drift towards each other roughly along $\hat{k}_y$. At larger fields, a series of annihilation/creation events of DPs of opposite windings occurs. A key distinction here is that in the limit where the DPs are close to Γ_{M}, the lack of chiral symmetry permits a term $\propto \boldsymbol{B} \cdot \boldsymbol{k}$ to 'tilt' the approximate QBCP. Thus, while the details are more involved in the chiral limit, parallel fields can qualitatively modify the band structure even for realistic w_{AA}.

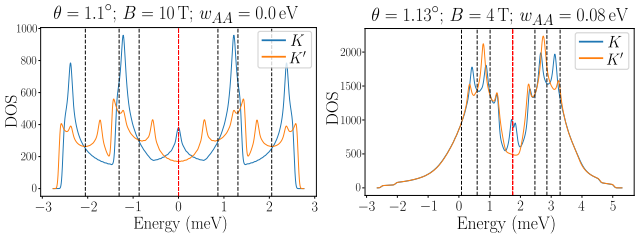

FIG. 3. Valley-resolved DOS of the central bands, including both orbital and spin effects. The magnetic field direction corresponds to the 'easy' direction for valley K. Red dashed line indicates charge neutrality, while black dashed lines indicate other integer fillings of the central bands (8 in total).

IV. DISCUSSION

The in-plane field acts asymmetrically on the two valleys. There will also be further splitting $\Delta E_s = g_s \mu_B B$ due to the spin Zeeman effect, where the spin g-factor $g_s \simeq 2$ for graphene systems [56, 57]. These four flavors should be considered together to get a fuller picture of the effect of B. A useful diagnostic here is the total density of states (DOS). The most significant orbital effect is to move DPs and tune the energy of their van Hove singularities. If these energies coincide with the Zeeman splitting, then valley-resolved features can appear in the DOS at charge neutrality. This is shown in Fig. 3 for both $w_{AA} = 0$ and $w_{AA} = 0.08$ eV, where a peak in the DOS for one of the valleys is apparent for $B \leq 10$ T. The shuffling of van Hove singularities is expected to have a direct impact on the metallic states and on their correlation-driven instabilities.

Many of the most intriguing aspects of TBG lie in the properties of its various correlated ground states. One class of such correlated insulators emerges after the opening of single-particle gaps due to interactions within the resulting Chern bands. For example, a partially aligned hexagonal boron nitride (hBN) substrate [13, 15, 58] on the top/bottom layer of TBG can be modeled by a uniform perturbation $\sim \Delta_{1(2)}\sigma_z$. This explicitly breaks $\hat{C}_{2\mathrm{v}}$ and therefore gaps out the DPs — the resulting bands have Chern numbers $C = 0, \pm 1$ depending on the sublattice-splitting strengths $\Delta_{1(2)}$ [25, 31]. Because of TRS, the Chern number configurations for the two valleys are opposite, which factors into the energetic balance between valley-polarized and intervalley coherent ground states at integer filling [25, 30, 31]. More exotic many-body phases have been proposed based on this single-particle starting point, such as excitonic quantum Hall states [59–61], as well as fractional Chern insulators at non-integer filling factors [62–64]. However, the magnetic field introduced here violates TRS, removing the constraints on C for the different valleys. This is demonstrated in Fig. 4, which shows that it is possible in principle to engineer a situation where one valley has $C = 0$ while the other has $|C| = 1$. Given the recent observation of orbital ferromagnetism and the resulting anomalous Hall effect in hBN-TBG, our work suggests that parallel fields can provide a new route to modifying the band topology

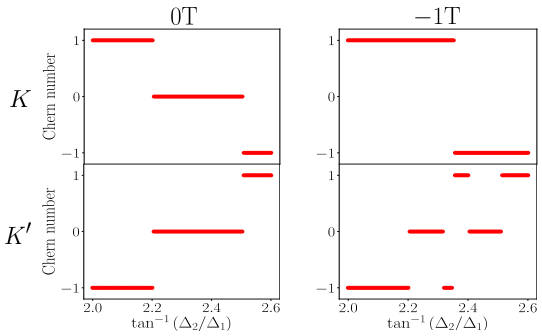

FIG. 4. Conduction band Chern number for $w_{AA} = 0.08$ meV and $\theta = 1.1°$, as a function of substrate configuration — the quantity $\sqrt{\Delta_1^2 + \Delta_2^2} = 10$ meV is held constant.

that underlies such correlated phases.

Even absent such substrate-induced effects, TBG still exhibits many correlation-driven phenomena. Here we note that *prima facie* the energy scales associated with a parallel field (0.3 meV $\cdot$ T^{-1}) compare favorably with the gaps ($0.1-1$ meV) reported for various experimentally realized insulating and superconducting states. It is therefore reasonable to imagine that it introduces a new energy scale that can tune the phase boundaries between different correlated phases. A potentially useful feature is that the effect of the parallel field on the DOS is valley- and spin- resolved. We also note that semimetallic behavior and novel correlated phases have been reported at charge neutrality, which is intriguing in light of the fact that this is where we anticipate the effect of a parallel field to be most dramatic. However, we caution that previous work [32] has considered the orbital effects of a parallel field on correlated insulating states at charge neutrality within a Hartree-Fock (HF) picture, and argued that these will be small since the HF bandstructure has its smallest gap at the Γ_M-point, where the electronic states do not directly couple to the parallel field. We suggest an alternative perspective, where the orbital shuffling of the single-particle states is taken into account *before* considering interactions. We defer a detailed exploration of these questions to the future, and here simply note that the delicate interplay of correlations and band structure suggests that the answers are likely subtle and worthy of further investigation.

ACKNOWLEDGMENTS

We thank B.A. Bernevig for useful discussions. We acknowledge support from the European Research Council (ERC) under the European Union Horizon 2020 Research and Innovation Programme [Grant Agreement No. 804213-TMCS] (SAP, YHK).

[1] S. A. Parameswaran, R. Roy, and S. L. Sondhi, Comptes Rendus Physique **14**, 816 (2013), topological insulators / Isolants topologiques.
[2] E. J. Bergholtz and Z. Liu, International Journal of Modern Physics B **27**, 1330017 (2013).
[3] A. K. Geim and I. V. Grigorieva, Nature **499**, 419 (2013).
[4] J. M. B. Lopes dos Santos, N. M. R. Peres, and A. H. Castro Neto, Phys. Rev. Lett. **99**, 256802 (2007).
[5] G. Trambly de Laissardière, D. Mayou, and L. Magaud, Nano letters **10**, 804 (2010).
[6] R. Bistritzer and A. H. MacDonald, Proceedings of the National Academy of Sciences **108**, 12233 (2011), https://www.pnas.org/content/108/30/12233.full.pdf.
[7] J. M. B. Lopes dos Santos, N. M. R. Peres, and A. H. Castro Neto, Phys. Rev. B **86**, 155449 (2012).
[8] P. San-Jose, J. González, and F. Guinea, Phys. Rev. Lett. **108**, 216802 (2012).
[9] G. Li, A. Luican, J. L. Dos Santos, A. C. Neto, A. Reina, J. Kong, and E. Andrei, Nature Physics **6**, 109 (2010).
[10] A. Luican, G. Li, A. Reina, J. Kong, R. R. Nair, K. S. Novoselov, A. K. Geim, and E. Y. Andrei, Phys. Rev. Lett. **106**, 126802 (2011).
[11] Y. Cao, V. Fatemi, A. Demir, S. Fang, S. L. Tomarken, J. Y. Luo, J. D. Sanchez-Yamagishi, K. Watanabe, T. Taniguchi, E. Kaxiras, *et al.*, Nature **556**, 80 (2018).
[12] Y. Cao, V. Fatemi, S. Fang, K. Watanabe, T. Taniguchi, E. Kaxiras, and P. Jarillo-Herrero, Nature **556**, 43 (2018).
[13] A. L. Sharpe, E. J. Fox, A. W. Barnard, J. Finney, K. Watanabe, T. Taniguchi, M. A. Kastner, and D. Goldhaber-Gordon, Science **365**, 605 (2019), https://science.sciencemag.org/content/365/6453/605.full.pdf.
[14] X. Lu, P. Stepanov, W. Yang, M. Xie, M. A. Aamir, I. Das, C. Urgell, K. Watanabe, T. Taniguchi, G. Zhang, *et al.*, Nature **574**, 653 (2019).
[15] M. Serlin, C. L. Tschirhart, H. Polshyn, Y. Zhang, J. Zhu, K. Watanabe, T. Taniguchi, L. Balents, and A. F. Young, Science **367**, 900 (2020), https://science.sciencemag.org/content/367/6480/900.full.pdf.
[16] H. C. Po, L. Zou, A. Vishwanath, and T. Senthil, Phys. Rev. X **8**, 031089 (2018).
[17] L. Zou, H. C. Po, A. Vishwanath, and T. Senthil, Phys. Rev. B **98**, 085435 (2018).
[18] H. C. Po, L. Zou, T. Senthil, and A. Vishwanath, Phys. Rev. B **99**, 195455 (2019).
[19] J. Kang and O. Vafek, Phys. Rev. X **8**, 031088 (2018).
[20] M. Koshino, N. F. Q. Yuan, T. Koretsune, M. Ochi, K. Kuroki, and L. Fu, Phys. Rev. X **8**, 031087 (2018).
[21] C. Xu and L. Balents, Phys. Rev. Lett. **121**, 087001 (2018).
[22] N. F. Q. Yuan and L. Fu, Phys. Rev. B **98**, 045103 (2018).
[23] M. Xie and A. H. MacDonald, arXiv preprint arXiv:1812.04213 (2018).
[24] G. Tarnopolsky, A. J. Kruchkov, and A. Vishwanath, Phys. Rev. Lett. **122**, 106405 (2019).
[25] N. Bultinck, S. Chatterjee, and M. P. Zaletel, arXiv preprint arXiv:1901.08110 (2019).
[26] Z. Song, Z. Wang, W. Shi, G. Li, C. Fang, and B. A. Bernevig, Phys. Rev. Lett. **123**, 036401 (2019).
[27] B. Lian, Z. Wang, and B. A. Bernevig, Phys. Rev. Lett. **122**, 257002 (2019).
[28] A. Thomson, S. Chatterjee, S. Sachdev, and M. S. Scheurer, Phys.

Rev. B **98**, 075109 (2018).
[29] F. Wu, A. H. MacDonald, and I. Martin, Phys. Rev. Lett. **121**, 257001 (2018).
[30] Y.-H. Zhang, D. Mao, Y. Cao, P. Jarillo-Herrero, and T. Senthil, Phys. Rev. B **99**, 075127 (2019).
[31] Y.-H. Zhang, D. Mao, and T. Senthil, Phys. Rev. Research **1**, 033126 (2019).
[32] S. Liu, E. Khalaf, J. Y. Lee, and A. Vishwanath, arXiv e-prints , arXiv:1905.07409 (2019), arXiv:1905.07409 [cond-mat.str-el].
[33] F. Wu and S. Das Sarma, Phys. Rev. B **99**, 220507 (2019).
[34] T. Stauber, T. Low, and G. Gómez-Santos, Phys. Rev. Lett. **120**, 046801 (2018).
[35] T. Stauber, T. Low, and G. Gómez-Santos, Phys. Rev. B **98**, 195414 (2018).
[36] S. Carr, S. Fang, P. Jarillo-Herrero, and E. Kaxiras, Phys. Rev. B **98**, 085144 (2018).
[37] M. Yankowitz, S. Chen, H. Polshyn, Y. Zhang, K. Watanabe, T. Taniguchi, D. Graf, A. F. Young, and C. R. Dean, Science **363**, 1059 (2019), https://science.sciencemag.org/content/363/6431/1059.full.pdf.
[38] Y. Xie, B. Lian, B. Jäck, X. Liu, C.-L. Chiu, K. Watanabe, T. Taniguchi, B. A. Bernevig, and A. Yazdani, Nature **572**, 101 (2019).
[39] A. Kerelsky, L. J. McGilly, D. M. Kennes, L. Xian, M. Yankowitz, S. Chen, K. Watanabe, T. Taniguchi, J. Hone, C. Dean, *et al.*, Nature **572**, 95 (2019).
[40] Y. Choi, J. Kemmer, Y. Peng, A. Thomson, H. Arora, R. Polski, Y. Zhang, H. Ren, J. Alicea, G. Refael, *et al.*, Nature Physics , 1 (2019).
[41] Y. Jiang, X. Lai, K. Watanabe, T. Taniguchi, K. Haule, J. Mao, and E. Y. Andrei, Nature **573**, 91 (2019).
[42] B. Roy and K. Yang, Phys. Rev. B **88**, 241107 (2013).
[43] Y. D. Chong, X.-G. Wen, and M. Soljačić, Phys. Rev. B **77**, 235125 (2008).
[44] K. Sun, H. Yao, E. Fradkin, and S. A. Kivelson, Phys. Rev. Lett. **103**, 046811 (2009).
[45] The emergent periodicity arises because the intralayer physics is modelled by Dirac terms, which is a good approximation when $|\boldsymbol{k}-\boldsymbol{K}|a \ll 1$ (hence the "continuum" designation). If we include the full monolayer dispersion, this permits purely in-plane Bragg scattering by a graphene reciprocal lattice vector $\boldsymbol{b}_j$. In general, $\boldsymbol{b}_j$ may not be expressible as an integer sum of moiré reciprocal lattice vectors $\boldsymbol{b}_{\mathrm{M},j}$, which is equivalent to incommensurability.
[46] N. N. T. Nam and M. Koshino, Phys. Rev. B **96**, 075311 (2017).
[47] S. Carr, S. Fang, Z. Zhu, and E. Kaxiras, Phys. Rev. Research **1**, 013001 (2019).
[48] M. Goerbig and G. Montambaux, in *Dirac Matter* (Springer, 2017) pp. 25–53.
[49] R. de Gail, M. O. Goerbig, F. Guinea, G. Montambaux, and A. H. Castro Neto, Phys. Rev. B **84**, 045436 (2011).
[50] J. Ahn, S. Park, and B.-J. Yang, Phys. Rev. X **9**, 021013 (2019).
[51] More precisely we consider the limit of infinitesimal interlayer coupling, so that the gauges in each layer cannot be separately transformed.
[52] R. de Gail, M. O. Goerbig, and G. Montambaux, Phys. Rev. B **86**, 045407 (2012).
[53] R. de Gail, J.-N. Fuchs, M. Goerbig, F. Piéchon, and G. Montambaux, Physica B: Condensed Matter **407**, 1948 (2012), proceedings of the International Workshop on Electronic Crystals (ECRYS-2011).
[54] G. Montambaux, L.-K. Lim, J.-N. Fuchs, and F. Piéchon, Phys. Rev. Lett. **121**, 256402 (2018).
[55] E. McCann and V. I. Fal'ko, Phys. Rev. Lett. **96**, 086805 (2006).
[56] Y. J. Song, A. F. Otte, Y. Kuk, Y. Hu, D. B. Torrance, P. N. First, W. A. De Heer, H. Min, S. Adam, M. D. Stiles, *et al.*, Nature **467**, 185 (2010).
[57] E. V. Kurganova, H. J. van Elferen, A. McCollam, L. A. Ponomarenko, K. S. Novoselov, A. Veligura, B. J. van Wees, J. C. Maan, and U. Zeitler, Phys. Rev. B **84**, 121407 (2011).
[58] J. Jung, A. M. DaSilva, A. H. MacDonald, and S. Adam, Nature communications **6**, 6308 (2015).
[59] Y. H. Kwan, Y. Hu, S. H. Simon, and S. A. Parameswaran, "Excitonic fractional quantum hall hierarchy in moiré heterostructures," (2020), arXiv:2003.11559 [cond-mat.str-el].
[60] Y. H. Kwan, Y. Hu, S. H. Simon, and S. A. Parameswaran, "Exciton band topology in spontaneous quantum anomalous hall insulators: applications to twisted bilayer graphene," (2020), arXiv:2003.11560 [cond-mat.str-el].
[61] N. Stefanidis and I. Sodemann, "Excitonic laughlin states in ideal topological insulator flat bands and possible presence in moiré superlattice materials," (2020), arXiv:2004.03613 [cond-mat.str-el].
[62] A. Abouelkomsan, Z. Liu, and E. J. Bergholtz, Phys. Rev. Lett. **124**, 106803 (2020).
[63] P. J. Ledwith, G. Tarnopolsky, E. Khalaf, and A. Vishwanath, "Fractional chern insulator states in twisted bilayer graphene: An analytical approach," (2019), arXiv:1912.09634 [cond-mat.str-el].
[64] C. Repellin and T. Senthil, "Chern bands of twisted bilayer graphene: fractional chern insulators and spin phase transition," (2019), arXiv:1912.11469 [cond-mat.str-el].